JACS
JOURNAL OF THE AMERICAN CHEMICAL SOCIETY
Article
pubs.acs.org/JACS

Structural and Mechanistic Insights into Fast Lithium-Ion Conduction in Li_4SiO_4–Li_3PO_4 Solid Electrolytes

Yue Deng,[†,‡] Christopher Eames,[‡] Jean-Noël Chotard,[†] Fabien Lalère,[†] Vincent Seznec,[†] Steffen Emge,[§] Oliver Pecher,[§] Clare P. Grey,[§] Christian Masquelier,[†] and M. Saiful Islam*[,‡]

[†]Laboratoire de Réactivité et Chimie des Solides (UMR CNRS 7314), Université de Picardie Jules Verne, 33 rue Saint Leu, 80039 Amiens Cedex, France

[‡]Department of Chemistry, University of Bath, Bath BA2 7AY, U.K.

[§]Department of Chemistry, University of Cambridge, Cambridge CB2 1EW, U.K.

Supporting Information

ABSTRACT: Solid electrolytes that are chemically stable and have a high ionic conductivity would dramatically enhance the safety and operating lifespan of rechargeable lithium batteries. Here, we apply a multi-technique approach to the Li-ion conducting system $(1-z)Li_4SiO_4-(z)Li_3PO_4$ with the aim of developing a solid electrolyte with enhanced ionic conductivity. Previously unidentified superstructure and immiscibility features in high-purity samples are characterized by X-ray and neutron diffraction across a range of compositions (z = 0.0–1.0). Ionic conductivities from AC impedance measurements and large-scale molecular dynamics (MD) simulations are in good agreement, showing very low values in the parent phases (Li_4SiO_4 and Li_3PO_4) but orders of magnitude higher conductivities (10^{-3} S/cm at 573 K) in the mixed compositions. The MD simulations reveal new mechanistic insights into the mixed Si/P compositions in which Li-ion conduction occurs through 3D pathways and a cooperative interstitial mechanism; such correlated motion is a key factor in promoting high ionic conductivity. Solid-state ^{6}Li, ^{7}Li, and ^{31}P NMR experiments reveal enhanced local Li-ion dynamics and atomic disorder in the solid solutions, which are correlated to the ionic diffusivity. These unique insights will be valuable in developing strategies to optimize the ionic conductivity in this system and to identify next-generation solid electrolytes.

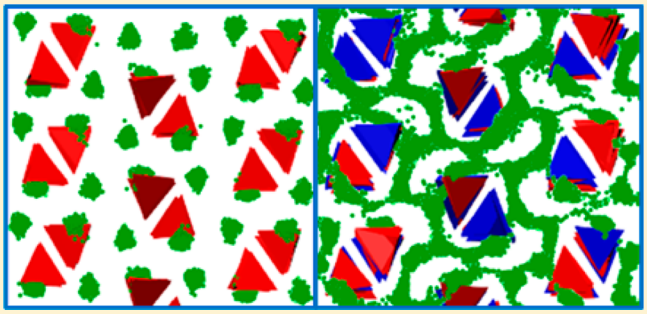

1. INTRODUCTION

The revolution in portable electronic devices has been powered by rechargeable lithium-ion batteries. Such batteries with liquid electrolytes, however, have cycle life and safety issues, whereas all-solid-state batteries with inorganic electrolytes may be regarded as a safer long-term solution.[1−6] Many structural families[7−12] have been investigated to identify potential ion-conducting solid electrolytes, including framework-type materials based on NASICON, LISICON, thio-LISICON, and garnet structures. Recently, a sulfur-based Li_2S–P_2S_5 glass–ceramic solid electrolyte has been reported to show an ionic conductivity (1.7×10^{-2} S/cm at room temperature) higher than those of many commonly used liquid electrolytes.[13] However, sulfide-based electrolytes are very hydroscopic[14] and must be prepared in a water-free environment. They also operate in limited voltage windows. Although oxides do not currently have as high ionic conductivity as sulfides, they exhibit higher stability and are easier to synthesize and handle.

The Li_4SiO_4–Li_3PO_4 solid solution system and the end-member parent phases have been identified as potential solid electrolytes,[15−27] but not all compositions have been fully characterized. It has been reported that the ionic conductivity can be increased by 3 orders of magnitude for $Li_{4-x}Si_{1-x}P_xO_4$ or γ-$Li_{3+y}Si_yP_{1-y}O_4$ compositions, compared with the two end members, Li_4SiO_4 and γ-Li_3PO_4.[18]

This drastic enhancement of conductivity is believed to be caused by the increased concentration of Li-ion vacancies in $Li_{4-x}Si_{1-x}P_xO_4$ and Li-ion interstitials in $Li_{3+y}Si_yP_{1-y}O_4$, with the ionic defects acting as charge carriers. However, an atomic-scale understanding of the conduction mechanisms and local structures in this system is still lacking; such detail is important for developing strategies for optimizing the conductivity, as well as identifying next-generation materials.

Both Li_4SiO_4 and γ-Li_3PO_4 are related to the LISICON-type structure with XO_4-based (X = Si or P) tetrahedral units (Figure 1), and Li–O polyhedra. The crystal structure of Li_4SiO_4 was initially reported[28] to be monoclinic (space group $P2_1/m$, with β very close to 90°) and to contain six partially occupied crystallographically independent lithium sites. However, in the correct description lithium sites are fully occupied, giving rise to a complex 7-fold superstructure.[29] γ-Li_3PO_4

Received: May 7, 2015
Published: June 29, 2015

DOI: 10.1021/jacs.5b04444
J. Am. Chem. Soc. 2015, 137, 9136–9145

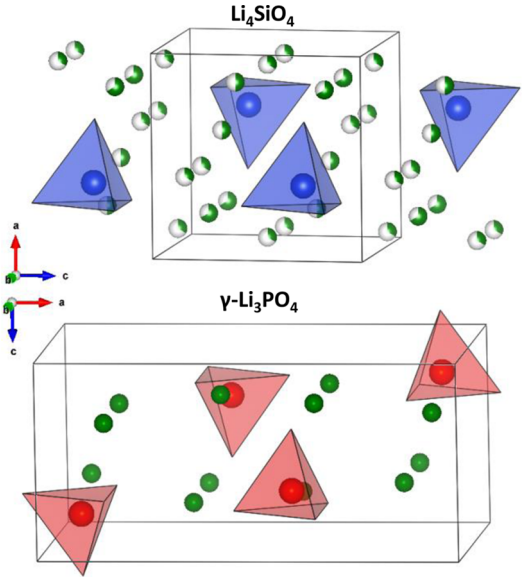

Figure 1. Schematic representations of the crystal structures of the end member phases Li_4SiO_4 (subcell) and γ-Li_3PO_4. Key: SiO_4 and PO_4, blue and red tetrahedra; lithium, green. Partially occupied Li sites are represented by partial shading. Unit cells are shown as solid lines.

crystallizes in a structure similar to Li_4SiO_4, but with orthorhombic symmetry (space group *Pnma*), as illustrated in Figure 1. The positions of the Si and P atoms are quite similar, but the respective orientations of the SiO_4 and PO_4 tetrahedra are different: up−down−up−down for Li_4SiO_4 and down−down−up−up for γ-Li_3PO_4 (along $a_P \approx 2c_{Si}$).

However, there have been limited structural studies of the complete solid solution. Early work by Hu[15] and West[30] determined that the Li_4SiO_4–Li_3PO_4 system did not yield one single continuous solid solution, as both end members do not possess the same crystal structure, despite being closely related to each other. More recent work by Arachi et al.[18] proposed solubility limits $x_{max} = 0.40$ for $Li_{4-x}Si_{1-x}P_xO_4$ and $y_{max} = 0.40$ for $Li_{3+y}Si_yP_{1-y}O_4$, while the existence of single-phase $Li_{3.5}Si_{0.5}P_{0.5}O_4$ remains uncertain.

Here, we investigate the crystal chemistry and ion transport properties of solid solution compositions within the Li_4SiO_4—Li_3PO_4 system, using a powerful combination of experimental and computational techniques. Very high purity Li_4SiO_4, $Li_{3.75}Si_{0.75}P_{0.25}O_4$, $Li_{3.5}Si_{0.5}P_{0.5}O_4$, $Li_{3.25}Si_{0.25}P_{0.75}O_4$, and γ-Li_3PO_4 samples were obtained and further investigated by various diffraction (single-crystal, powder X-ray, powder neutron) techniques. Solid-state ^{6}Li, ^{7}Li, and ^{31}P NMR spectroscopy is used to provide insights into local structural ordering and Li-ion dynamics. The crystal structures and ion transport are then investigated by atomistic molecular dynamics (MD) techniques, in which the relative energies of possible defect arrangements are considered, as well as large-scale simulations of ion transport mechanisms.

2. METHODS

2.1. Synthesis. The raw materials used in this work were all purchased from Sigma-Aldrich, including $LiOH·H_2O$ (98%), SiO_2 (fumed, dried at 500 °C for 3 h) and β-Li_3PO_4 powders. Stoichiometric mixtures of raw materials were dispersed in distilled water, the quantity of which was adjusted to give an overall concentration of 0.6 mol of Li per liter of H_2O. The solution was then slowly heated to 80 °C to evaporate water. The resulting solid was pulverized and cold-pressed into pellets under 40 MPa. The pellets were then heated in alumina combustion crucibles at 900 °C for 10 h under Ar flow, followed by slow cooling to room temperature, and then pulverized. Energy-dispersive X-ray (EDX) analysis indicated no contamination of Al from the crucible. Scanning electron microscopy showed that the synthesized samples consist of aggregates of about 100 μm in size and smaller individual particles of about 10−50 μm. Since these samples are quite reactive with CO_2,[31] they were stored in a glovebox. Single crystals of Li_4SiO_4 were prepared by a similar method, except that the final heating temperature was set to 1200 °C, and the cooling rate was set to 10 °C/h. To produce pure γ-Li_3PO_4, commercially available β-Li_3PO_4 was heated at 850 °C for 10 h, cooled to room temperature, and pulverized.

2.2. Diffraction. X-ray powder diffraction (XRPD) patterns were collected from a Bruker D8 diffractometer (Cu Kα radiation, θ−θ configuration). High-quality diffraction patterns were recorded overnight over 2θ ranges of 10−100°, with a step size of 0.009° and a scan rate of 3.8 s/step. For $Li_{3.75}Si_{0.75}P_{0.25}O_4$, a neutron powder diffraction experiment was carried out at the SINQ spallation source[32] of the Paul Scherrer Institute (Switzerland) using the high-resolution neutron diffractometer HRPT[33] (λ = 1.494 Å). Neutron powder diffraction patterns were collected for $Li_{3.5}Si_{0.5}P_{0.5}O_4$ and $Li_{3.25}Si_{0.25}P_{0.75}O_4$ using the high-resolution D2B diffractometer at Institute Laue-Langevin (Grenoble, France). High-quality diffraction patterns were recorded over 2θ ranges of 10−160°, with a step size of 0.05°, accumulated over 6 h. Single-crystal X-ray diffraction (XRD) measurements were carried out at 293 K using a Bruker D8 Venture diffractometer, with Mo Kα radiation (multilayer optics monochromator). Data collection conditions, crystal data, and refinement parameters are listed in the Supporting Information (SI), Table S1.

2.3. AC Impedance Spectroscopy. For ionic conductivity measurements, powders of Li_4SiO_4, Li_3PO_4, and their solid solutions were cold-pressed into disk-shaped pellets. In each case, about 150 mg of powder was placed in a graphite matrix (10 mm in diameter) and cold-pressed at 40 MPa. The pellets were then sintered in a FCT Spark Plasma Sintering apparatus at 70 K min^{-1} up to 700 °C for 3 min under an applied force of 8 kN. The resulting dense pellets were polished and metalized on both sides by gold sputtering using a Bal-Tec SCD 050. The sintering process and metallization step were carried out in an Ar atmosphere. Pellets were then dried under primary vacuum at 100 °C overnight before measurements and immediately transferred into a glovebox. The sample was then introduced into the impedance measurement cell directly in the glovebox to avoid any air contamination. Impedance measurements were performed over a frequency range of 0.1 Hz to 200 kHz, between 25 and 300 °C, both upon heating and upon cooling, under static Ar.[34]

2.4. Solid-State NMR Spectroscopy. Powder samples of Li_4SiO_4, $Li_{3.75}Si_{0.75}P_{0.25}O_4$, $Li_{3.5}Si_{0.5}P_{0.5}O_4$, and $Li_{3.25}Si_{0.25}P_{0.75}O_4$, and Li_3PO_4 were packed in 1.3, 4.0, or 7.0 mm ZrO_2 rotors (Bruker) and closed with Kel-F or BN caps, depending on the temperature of the experiment. All sample handling was done under an Ar atmosphere in a glovebox with $p(H_2O,O_2) < 0.1$ ppm. Ambient and high-temperature (320−875 K) ^{7}Li magic angle spinning (MAS) NMR experiments were performed at 9.4 T (Avance I console) using a Bruker double-resonance 7.0 mm MAS probe with laser heating of the sample. Temperature calibration using KBr was done before measuring the samples. ^{7}Li NMR signal line shapes were determined by one-pulse experiments with high-power pulses of 2.1 μs (7.0 mm MAS) and 0.9 μs (4.0 mm MAS) and a repetition time of 5.0 s. A saturation recovery pulse sequence was applied to determine ^{7}Li spin−lattice relaxation time constants (T_1) at variable temperatures. Ambient temperature ^{6}Li MAS NMR experiments were performed at 11.7 T (Avance III HD console) using a Bruker triple-resonance 4.0 mm MAS probe, including a temperature calibration on the ^{207}Pb shift in lead nitrate before the actual experiment.[35] ^{6}Li pulse optimization was done on $^6Li_2CO_3$ and followed by NMR signal line shape measurements on $Li_{3.75}Si_{0.75}P_{0.25}O_4$, $Li_{3.5}Si_{0.5}P_{0.5}O_4$, and $Li_{3.25}Si_{0.25}P_{0.75}O_4$ using a one-pulse sequence with high-power pulses of 4.45 μs and a repetition time of 25 s. The ^{6}Li and ^{7}Li NMR shifts were referenced to a 1 M LiCl solution in D_2O.[36] Activation energies were derived by both

DOI: 10.1021/jacs.5b04444
J. Am. Chem. Soc. 2015, 137, 9136−9145

Bloembergen–Purcell–Pound (BPP) fits[37,38] and fitting of the linear regimes in Arrhenius plots (SI, Table S2). Due to the low natural abundance of ^{6}Li (7.59%) vs ^{7}Li (92.41%)[36] and the significantly longer relaxation times, we focused on ^{7}Li NMR experiments in this study for the sake of higher sensitivity and shorter measurement times. ^{31}P MAS NMR experiments were performed at ambient temperature in a magnetic field of 16.4 T using a Bruker 1.3 mm triple-resonance MAS probe on an Avance III console. Pulse optimization was done using ammonium dihydrogen phosphate (ADP).[39] A one-pulse sequence with high-power 1.8 μs pulses and a recycle delay of 3.0 s was applied to acquire the spectra for the line-shape measurements. The ^{31}P NMR signals were referenced to 85% H_3PO_4.[36]

2.5. Atomistic Modeling. Interatomic potentials-based methods, which are well established and detailed elsewhere, were employed.[40−43] The effective potentials describing the interatomic forces include a long-range Coulomb term, short-range Morse function, and repulsive contribution. The parameters were taken from the extensive library of potentials developed by Pedone et al.,[44] which have been shown to perform well in MD simulations of silicates and polyanion-type materials. Further details can be found in the SI, Table S3. Modeling of crystal structures and different defect ordering schemes was carried out using energy minimization methods (GULP code[41,45]). For ion diffusion modeling we have used MD methods (DL_POLY 4 code[42]). A time step of 1 fs for MD runs of up to 5 ns with supercells containing 20 000–30 000 ions was employed. Simulations were carried out at several temperatures (300–673 K). Each set of calculations was repeated three times to confirm good statistics. Such computational methods have been applied successfully to other Li-ion battery materials.[43,46−53] To facilitate comparison with experimental data, the calculated diffusion coefficients (D) were used to derive the ionic conductivity σ using the Nernst–Einstein relationship

$$\frac{\sigma}{D} = H_R \frac{nq^2}{kT} \quad (1)$$

where n is the number of particles per unit volume, q is the charge of an electron, k is the Boltzmann constant, and T is the temperature. H_R is the correlation factor (or Haven ratio), defined as the ratio of the tracer diffusion coefficient to a diffusion coefficient dependent upon the ionic conductivity. In this work we have used the methods of Morgan and Madden[54] to determine H_R. A Haven ratio of 1.0 suggests uncorrelated ion hopping, whereas high values (>2) are observed in fast-ion conductors with highly correlated ionic motion.

3. RESULTS AND DISCUSSION

3.1. Structures of $(1-z)Li_4SiO_4-(z)Li_3PO_4$ Solid Solutions. Our study confirms that the compositions Li_4SiO_4 and $Li_{3.75}Si_{0.75}P_{0.25}O_4$ can be indexed in space group $P2_1/m$, while $Li_{3.5}Si_{0.5}P_{0.5}O_4$ and $Li_{3.25}Si_{0.25}P_{0.75}O_4$ adopt the γ-Li_3PO_4 structure (Figure 2a). Lattice parameters refined from XRPD data are collected in Table 1.

To obtain deeper insights into the phase stabilities within the Li_4SiO_4–Li_3PO_4 system, we prepared several $(1-z)Li_4SiO_4-(z)Li_3PO_4$ compositions in steps of $\Delta z = 0.1$. We found that the immiscibility zone is around $0.35 < z < 0.45$. Between the two end members, the a, b, and c parameters vary smoothly except for an abrupt discontinuity between the a parameter of the P-substituted Li_4SiO_4 structure type and the c parameter of the Si-substituted Li_3PO_4 phase at $z = 0.4$, where two phases coexist (Figure 2b; note that $c_P \approx a_{Si}$).

The XRPD pattern of Li_4SiO_4 was indexed and the lattice parameters were refined using the unit cell proposed by Völlenkle[28] in the monoclinic space group $P2_1/m$. Most of the diffraction peaks of our sample could be indexed, but, as shown in Figure 3, many small-intensity contributions remained unidentified. These are signatures of lithium ordering within Li_4SiO_4 producing the supercell previously reported from

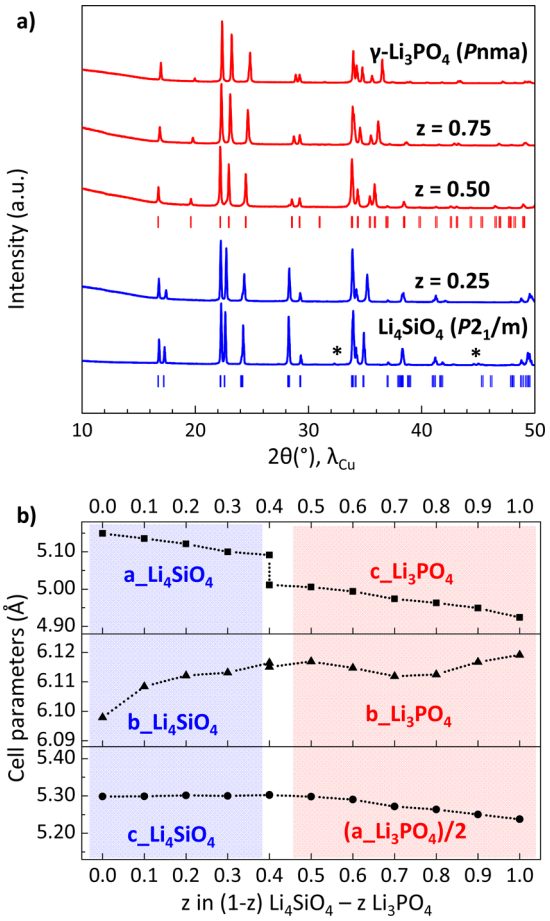

Figure 2. (a) XRPD patterns of powders obtained for the Li_4SiO_4–Li_3PO_4 system. Li_4SiO_4-based patterns are in blue; Li_3PO_4-based patterns are in red. Asterisks (*) indicate superstructure peaks. (b) Variation of lattice parameters as a function of z in $(1-z)Li_4SiO_4-(z)Li_3PO_4$.

single-crystal diffraction work[29] and seen here for the first time in XRPD data.

Tranqui et al.[29] described the structure of Li_4SiO_4 using the $P2_1/m$ space group (a = 11.546 Å, b = 6.090 Å, c = 16.645 Å, β = 99.5°, and Z = 14). The structure contains SiO_4 tetrahedra and LiO_n (n = 4, 5, 6) polyhedra. The 19 fully occupied crystallographic sites for Li are distributed over 9 4f Wyckoff positions, while the other 10 are at 2e positions; this results in 56 lithium atoms per unit cell. A similar structure was proposed by de Jong,[55] using results from single-crystal XRD and XPS measurements. Their structure was basically the same as that in previous work, with the main difference being the splitting of the Li(51) and Li(65) sites (using the notation of Tranqui) over two additional sites. It is noted that these sites in Tranqui's work[29] had thermal displacement parameters of 4.79 and 4.04 Å^2, respectively, approximately twice as large as those for the other Li atoms. All four positions then have an occupancy of 0.5, which introduces a small degree of positional disorder over the Li sublattice.

Careful inspection of our Li_4SiO_4 powder revealed that it contained single crystals of sufficient size (~20 μm) for precise structural analysis. Our refined structure contains 19 independent lithium sites. The corresponding Li(51) and Li(65) sites display isotropic thermal displacement parameters as high as 6.48 and 3.21 Å^2, indicating that these two lithium

DOI: 10.1021/jacs.5b04444
J. Am. Chem. Soc. 2015, 137, 9136–9145

Table 1. Cell Parameters Determined from X-ray Powder Diffraction for the $(1-z)Li_4SiO_4-(z)Li_3PO_4$ System

	Li_4SiO_4 (z = 0)[a]	z = 0.25	z = 0.50	z = 0.75	Li_3PO_4 (z = 1)
space group	$P2_1/m$	$P2_1/m$	*Pnma*	*Pnma*	*Pnma*
a (Å)	5.1504(3)	5.1094(2)	10.5990(7)	10.5356(3)	10.4763(3)
b (Å)	6.1012(4)	6.1135(4)	6.1155(4)	6.1169(2)	6.1193(2)
c (Å)	5.2998(3)	5.3002(4)	5.0114(3)	4.9697(2)	4.9245(2)
β (deg)	90.321(5)	90.378(4)	90	90	90
V/Z (Å^3)	83.268(3)	82.777(2)	81.207(2)	80.067(2)	78.924(2)

[a]Subcell parameters of Li_4SiO_4 are used for ease of comparison.

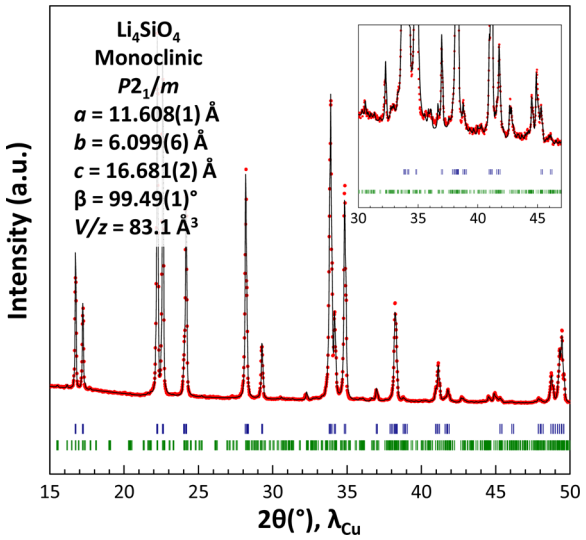

Figure 3. Full pattern profile matching of XRPD pattern of Li_4SiO_4: red dots, experimental data; black line, profile matching; blue bar, Bragg positions of the small cell; green bar, Bragg positions of the 7-fold super cell.

ions are loosely bound to their ideal positions. We carried out a second set of refinements by splitting the two sites. This resulted in occupancy factors for the sites split from Li(51) of 0.528(13) and 0.472(13) (and 0.73 Å from each other). The Li(65) was split into two sites, separated by 0.40 Å, with occupancies of 0.520(12) and 0.480(12).

Within the $Li_4SiO_4-Li_3PO_4$ system, only the $Li_{3.75}Si_{0.75}P_{0.25}O_4$ composition has been previously investigated[56] by single-crystal XRD. The refinement converged to an overall composition of $Li_{3.43}Si_{0.75}P_{0.25}O_4$ after summation of individual Li site occupancy factors. We determined the crystal structures of the three solid solution compositions $Li_{3.75}Si_{0.75}P_{0.25}O_4$, $Li_{3.5}Si_{0.5}P_{0.5}O_4$, and $Li_{3.25}Si_{0.25}P_{0.75}O_4$ through Rietveld refinements of neutron powder diffraction data. Unlike Li_4SiO_4, these three compositions do not exhibit long-range ordering of lithium ions at room temperature and therefore can be described using the original unit cells in Table 1.

The published atomic coordinates of each structure type (Li_4SiO_4 or γ-Li_3PO_4 (ICSD-77095)[57]) were used as starting models for the refinements of $Li_{3.75}Si_{0.75}P_{0.25}O_4$, $Li_{3.5}Si_{0.5}P_{0.5}O_4$, and $Li_{3.25}Si_{0.25}P_{0.75}O_4$ compositions. The main challenge here was to localize the lithium atomic positions and occupancy factors. The refinement strategy can be illustrated using $Li_{3.5}Si_{0.5}P_{0.5}O_4$ as an example. γ-Li_3PO_4 contains four formula units per unit cell, with one type of PO_4 tetrahedron and two crystallographically independent Li sites, Li1(8*d*) and Li2(4*c*), giving 12 lithium atoms per unit cell. We first verified that the Li1 and Li2 sites of Li_3PO_4 were appropriate for describing the structure of $Li_{3.5}Si_{0.5}P_{0.5}O_4$ by removing one or the other from the list of atomic coordinates and calculating Fourier transformed scattering density difference maps (Figure 4).

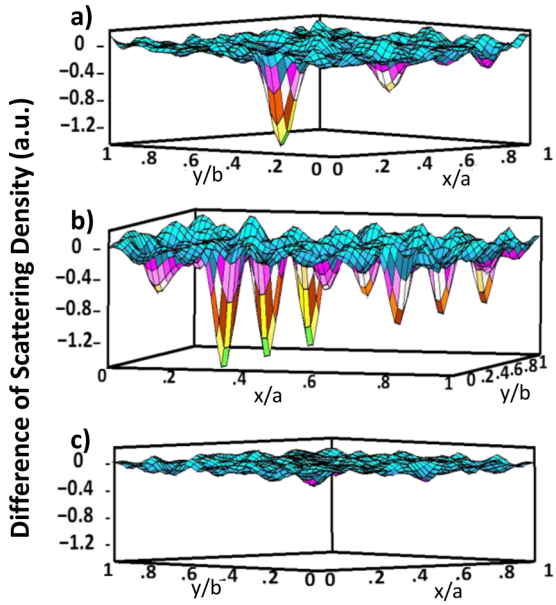

Figure 4. Fourier-transformed scattering density difference maps (at z = 0.7) from refinements of $Li_{3.5}Si_{0.5}P_{0.5}O_4$ neutron diffraction data (a) in the absence of Li1, (b) in the absence of Li2, and (c) with both Li1 and Li2.

These maps clearly reveal sharp difference density peaks at the atomic positions of Li1 and Li2, which were then subsequently used to refine the overall structure, as well as other positions in the unit cell.

In order to determine the positions of the last two Li atoms in the unit cell, two models were used to refine the structure. The first straightforward "3Li" model was based on the previous "2Li" model, with a third Li crystallographic position added where the Fourier-transformed scattering density difference map had the sharpest peak. A second "6Li" model was used as a starting configuration, based on the knowledge that the nonequivalent structure of $Li_{3.75}Si_{0.75}P_{0.25}O_4$ contains six crystallographically different lithium sites. In both cases, the refinements of cell parameters, atomic positions, and anisotropic thermal factors (B_{aniso}) of Si, P, and O gave reasonable values. The refinement of the isotropic thermal factor B_{iso} of Li(3) in the "3Li" model or Li(6) in the "6Li" model led to a divergence attributed to the low occupancy of the sites. Rietveld refinements resulted in a final value of the Bragg R-factor of 6.13% for the "3Li" model and 4.92% for the "6Li" model. The diffraction pattern and refinement results for

DOI: 10.1021/jacs.5b04444
J. Am. Chem. Soc. 2015, 137, 9136−9145

the "6Li" model, finally chosen as the most reliable one, are shown in Figure 5 and in SI, Table S4.

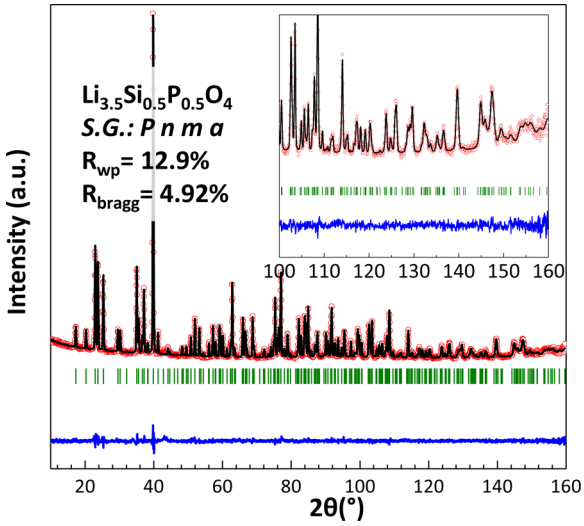

Figure 5. Neutron powder diffraction pattern and Rietveld refinement of $Li_{3.5}Si_{0.5}P_{0.5}O_4$.

Similar studies were carried out to determine the crystal structures of $Li_{3.75}Si_{0.75}P_{0.25}O_4$ and $Li_{3.25}Si_{0.25}P_{0.75}O_4$ (data summarized in SI, Tables S5 and S6, respectively). All of these compositions show highly symmetrical XO_4 tetrahedra ($Si_{1-z}P_zO_4$) with very small variation in the X−O bond lengths and O−X−O angles very close to 109.47°. Baur's polyhedral bond length distortion indices[58] are 0.5% for z = 0.25, 0.2% for z = 0.5, and 0.2% for z = 0.75, which are close to the usual value of 0.5% found in orthophosphates. The variation of the average X−O bond length with z in $Si_{1-z}P_zO_4$ tetrahedra is in excellent agreement with those obtained from linear interpolation between the average Si−O distance in Li_4SiO_4 and the average P−O distance in Li_3PO_4 (SI, Table S7). This further indicates that the experimental Si/P stoichiometry of the powders is very close to the nominal one. A detailed list of Li−O bond lengths can be found in SI, Table S4. The longer average Li−O distance around Li(6) (2.25 Å) is consistent with its lower occupancy factor (0.14). LiO_n face- and edge-sharing polyhedra are interconnected so as to generate a 3D conducting network.

^{7}Li MAS NMR experiments at ambient temperature reveal one NMR signal with respective rotational sidebands for the solid solutions and the end members (SI, Figure S8). A slight increase of the central transition's (CT's) full width at half-maximum (fwhm) indicates Li disorder in the solid solution phases. The detection of only one Li signal, although up to six different crystallographic positions are present in the solid solution structures, suggests chemically similar Li environments on the local atomic scale of NMR. The ^{7}Li homonuclear coupling and distribution of local environments prevent resonances from individual crystallographic sites from being resolved.

Variable-temperature (VT) ^{7}Li NMR signal line shapes of $Li_{3.75}Si_{0.75}P_{0.25}O_4$, $Li_{3.5}Si_{0.5}P_{0.5}O_4$, and $Li_{3.25}Si_{0.25}P_{0.75}O_4$ show a significant change of the broadening and intensity of the rotational sidebands as well as the CT's fwhm (Figure 6 and SI, Figure S9). Different regimes of Li motion and Li−Li couplings are revealed for different temperatures.

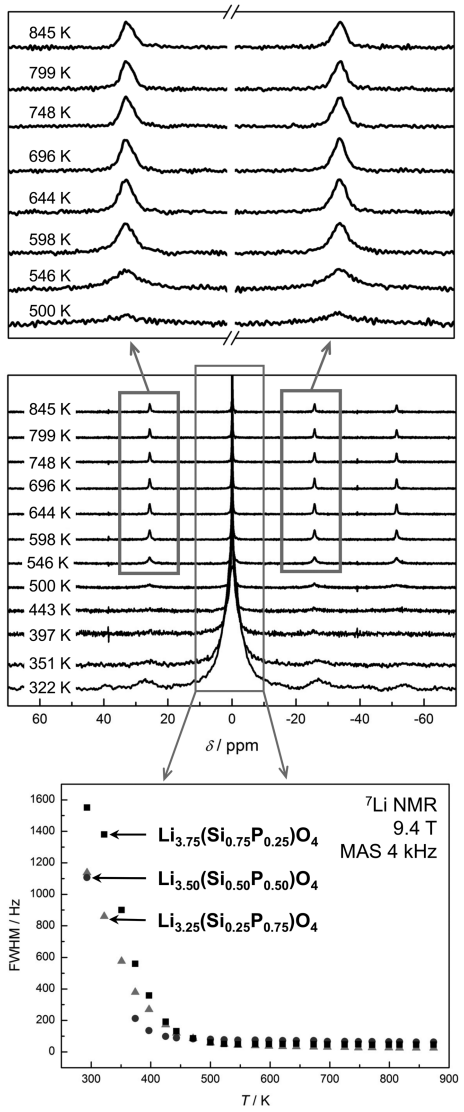

Figure 6. ^{7}Li VT MAS (4 kHz) NMR signals at 9.4 T. The middle graph shows the full spectra for $Li_{3.25}Si_{0.25}P_{0.75}O_4$ with a zoom of the first rotational sidebands at high temperatures (top). Temperature-dependent ^{7}Li fwhm values of the CT signals are depicted at the bottom for all samples.

^{6}Li MAS NMR spectra of the mixed compositions show higher experimental resolution than the ^{7}Li NMR spectra (SI, Figure S10). For $Li_{3.75}Si_{0.75}P_{0.25}O_4$, the spectrum contains four resonances at −0.67, 0.28, 0.67, and 1.58 ppm and is qualitatively similar to that obtained in previous work on the lithium orthosilicate.[59−61] The resonances were assigned to LiO_n environments with n = 6, 5, 4 and 3 from low to high frequencies (SI, Figure S10). The resolution decreases upon further P substitution in $Li_{3.5}Si_{0.5}P_{0.5}O_4$. The ^{6}Li NMR signal features are smeared out and shifted to the frequency range of the LiO_4 and LiO_5 environments. The LiO_6 and LiO_3 environments are no longer resolved, which agrees well with the Li−O distances and the respective LiO_n coordination for this composition (see SI, Table S4). Of note, however, is a further shift of the ^{6}Li NMR spectra for $Li_{3.25}Si_{0.25}P_{0.75}O_4$ to lower frequencies while showing higher resolution. At least three resonances at −0.31, 0.05, and 0.16 ppm are resolved (SI, Figure S10), indicating a different coordination. The ^{6}Li NMR experiments and the respective assignments of LiO_n environ-

DOI: 10.1021/jacs.5b04444
J. Am. Chem. Soc. 2015, 137, 9136−9145

Table 2. Comparison of Calculated Structural Parameters with Diffraction Data for $(1-z)Li_4SiO_4-(z)Li_3PO_4$

	z = 0.0		z = 0.5		z = 1.0	
	expt	calcd	expt	calcd	expt	calcd
a (Å)	11.555	11.500	10.589	10.636	10.490	10.563
b (Å)	6.099	6.162	6.115	6.119	6.120	6.229
c (Å)	16.730	16.932	5.006	5.072	4.927	5.020
β (deg)	99.06	100.84	90	90	90	90
Si/P−O (Å)	1.641	1.602	1.587	1.563	1.544	1.520
Li−O (Å)	2.050	2.078	2.080	1.974	1.968	2.022

ments reveal a decrease of the coordination number with increasing P substitution. This indicates a disperse distribution of the Li atoms ("liquid-like") with a mobile sublattice of the LiO_n polyhedra that is highly disordered.

^{31}P high-speed MAS NMR data revealed one signal for the pure phosphate Li_3PO_4 with 145 Hz in fwhm of 8.9(1) ppm, which is in line with the crystal structure (SI, Figure S11). A significant broadening of the line shapes with fwhm of 656, 626, and 489 Hz for $Li_{3.75}Si_{0.75}P_{0.25}O_4$, $Li_{3.5}Si_{0.5}P_{0.5}O_4$, and $Li_{3.25}Si_{0.25}P_{0.75}O_4$, respectively, indicates atomic disorder due to the mixed occupancies of the Si/P sites.

Only slight shift variations with respect to the Si/P occupancy are found, in line with previous ^{31}P NMR measurements.[62] The highest shift and a pronounced asymmetry are found for $Li_{3.5}Si_{0.5}P_{0.5}O_4$, indicating local atomic ordering that is more complex than the spatially averaged picture derived from diffraction. Slower MAS rates do not influence the ^{31}P NMR signal line shape and give identical shift values (SI, Figure S11).

For the atomistic simulations of ionic conduction in these mixed silicate−phosphates, it is essential to accurately model their crystal structures. In order to model the Li and Si/P fractional occupancies, numerous (>10 000) structure models were first energy minimized using random distributions of Li, Si, and P on their respective sites to find low-energy configurations. Calculated and observed structural parameters are given in Table 2 for the two end-member phases, Li_4SiO_4 and Li_3PO_4, and for $Li_{3.5}Si_{0.5}P_{0.5}O_4$ (data for $Li_{3.75}Si_{0.75}P_{0.25}O_4$ and $Li_{3.25}Si_{0.25}P_{0.75}O_4$ are listed in SI, Table S12). The calculated cell parameters and mean bond lengths deviate from experiment by at most 2%, and in most cases much less. Overall, the good reproduction of these complex structures of numerous different compositions gives us confidence that both the structural models and the interatomic potentials can be used reliably in the MD calculations.

3.2. Li-Ion Conductivity and Dynamics. Examination of Li^+ diffusion rates and conductivity is important for predicting battery charge/discharge rates, which we investigated using MD, AC impedance, and NMR spectroscopy. MD techniques are well suited to probing transport mechanisms at the atomic level, especially cooperative or correlated ion motion. Here, MD calculations over long simulation times of up to 5 ns were carried out over a temperature range covering typical battery operating temperatures for all compositions.

First, the mean-squared displacements (MSDs), $\langle r_i^2(t)\rangle$, of all lithium ions (Figure 7) show that Li^+ diffusion is significantly higher in the mixed PO_4/SiO_4 compositions than in the two end members. The Li^+ diffusion coefficient (D_{Li}) can be derived from the MSD data according to $\langle r_i^2(t)\rangle = 6D_it + B_i$. We calculate D_{Li} values of 2×10^{-9} and 2×10^{-12} cm^2/s for Li_4SiO_4 and Li_3PO_4, respectively, at 573 K, with higher values for the mixed compositions (for example, 4×10^{-8} cm^2/s for $Li_{3.75}Si_{0.75}P_{0.25}O_4$).

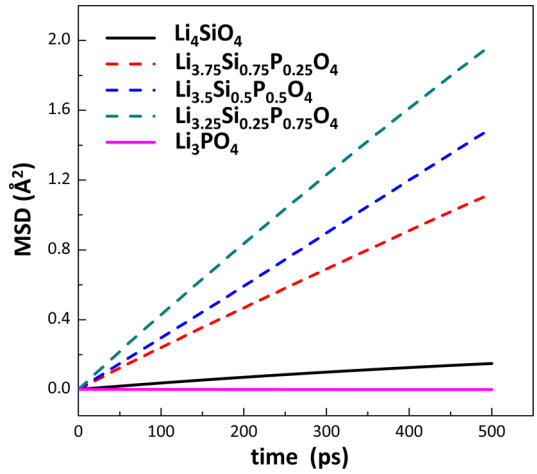

Figure 7. Mean-squared displacement (MSD) plots for Li^+ for the different compositions at 573 K. Full lines indicate end members, while dashed lines represent intermediate compositions.

Calculated ionic conductivities are compared with experimental values from our AC impedance measurements in Figure 8 (the AC impedance spectra are shown in SI, Figure S13). The trends and magnitude of the ionic conductivities of all compositions are highly compatible and show that the formation of solid solutions increases the ionic conductivity by 3−4 orders of magnitude compared to the two end members; for example, at 573 K, the three intermediate compounds have conductivities of about 2.5×10^{-3} S/cm, while the ionic

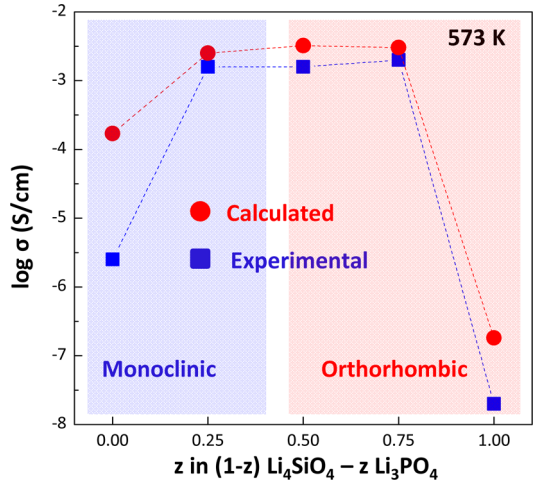

Figure 8. Experimental (blue squares) and calculated (red circles) ionic conductivities for the $Li_4SiO_4-Li_3PO_4$ system at 573 K.

DOI: 10.1021/jacs.5b04444
J. Am. Chem. Soc. 2015, 137, 9136−9145

conductivity is 2.5×10^{-6} S/cm for Li_4SiO_4 and 1.2×10^{-8} S/cm for Li_3PO_4.

For the intermediate compositions, conductivity values obtained from MD calculations (red circles in Figure 8) show good agreement with experimental values. For the end members, the calculated ionic conductivities are higher than those observed experimentally, especially for Li_4SiO_4. This difference is most likely due to these materials being poor ionic conductors with very slow lithium-ion diffusion, which did not reach the fully equilibrated state during the long MD simulations. Nevertheless, the trend in ionic conductivities across the composition range is well reproduced.

^{7}Li MAS NMR reveals much smaller spin−lattice relaxation times (T_1) of 3.60, 2.07, and 1.37 s for $Li_{3.75}Si_{0.75}P_{0.25}O_4$, $Li_{3.5}Si_{0.5}P_{0.5}O_4$, and $Li_{3.25}Si_{0.25}P_{0.75}O_4$, respectively, compared to 42.4 s for Li_3PO_4 and 21.2 s for Li_4SiO_4; these results suggest enhanced Li-ion dynamics in the solid solutions, in agreement with the impedance and modeling results. ^{7}Li VT T_1 measurements for the solid solution samples show a high temperature T_1 minimum that is in line with literature data for samples of similar composition (Figure 9 and SI, Figure S14).[37,38] Furthermore, the asymmetry of the slopes below and above the T_1 minima are in agreement with previous results for fast ion conductors.[59] A determination of the respective activation energies via a BPP fit gives 0.18(3), 0.23(2), and 0.21(2) eV for $Li_{3.75}Si_{0.75}P_{0.25}O_4$, $Li_{3.5}Si_{0.5}P_{0.5}O_4$, and $Li_{3.25}Si_{0.25}P_{0.75}O_4$, respectively (Figure 11, and SI, Tables S2 and S15). These values are lower than those from previous NMR measurements,[37,38,59] which is likely due to their slightly different compositions as well as the alternative synthesis routes.

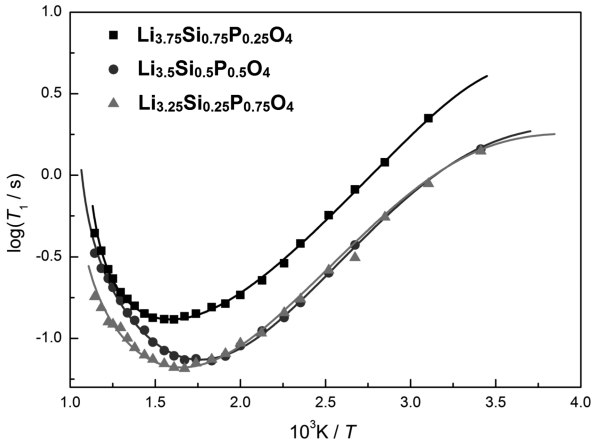

Figure 9. BPP fits of the T_1 data derived from ^{7}Li VT measurements at 9.4 T (MAS 4 kHz, 320−875 K).

Activation energies have also been derived from MD simulations (SI, Figure S16) and AC impedance measurements from Arrhenius plots (SI, Figure S17); a representative example is shown in Figure 10. Their values are listed together with BPP fitted values in SI, Table S15, and the results from the three techniques are summarized in Figure 11. In general, the results for the mixed compositions from all techniques demonstrate the same trends with much lower activation energies than the two end members. The absolute values of the activation energies, however, are sensitive to different length scales and degrees of long-range order probed by each technique. NMR T_1 data is highly sensitive to local ion

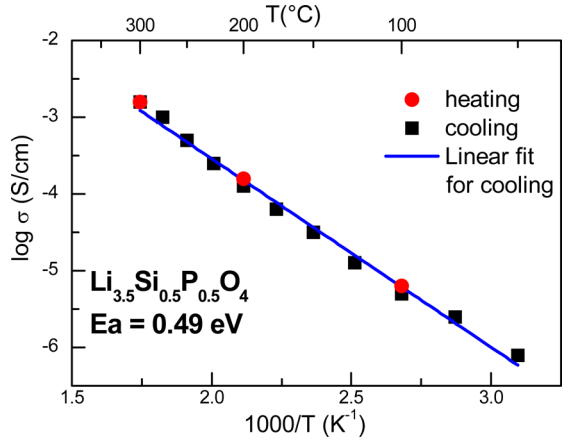

Figure 10. Arrhenius plot from AC impedance measurements for $Li_{3.5}Si_{0.5}P_{0.5}O_4$ (as a representative example). Data were recorded upon heating (red circles) and cooling (black squares). The activation energy was derived from a linear fit of data from cooling process (blue line).

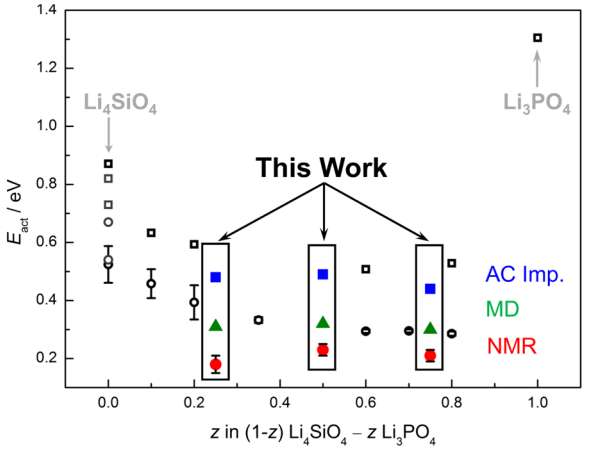

Figure 11. Activation energies E_{act} derived from conductivity (squares), NMR T_1 (circles) measurements and MD modeling (triangles). Data from previous studies[37,38,59] are in black. The scatter in E_{act} values for Li_4SiO_4 is likely due to differences in the data derived from impedance (Asai et al.,[37] Xu et al.[59]) and 1D NMR (Asai et al.,[37] Xu et al.[59]) as well as 2D NMR (Xu et al.[59]).

hopping such as the rapid oscillation over the low energy barrier between the split Li sites. In MD this local oscillatory behavior is averaged out and only long-range ionic transport in the bulk contributes, whereas AC impedance contains contributions from the entire sample, including grain boundary resistance.

On the basis of the BPP fit of the VT ^{7}Li NMR data and the respective correlation times τ_C at 573 K, we derived average jump rates for the Li atoms of 0.76, 1.49, and 1.18 GHz for the solid solutions $Li_{3.75}Si_{0.75}P_{0.25}O_4$, $Li_{3.5}Si_{0.5}P_{0.5}O_4$, and $Li_{3.25}Si_{0.25}P_{0.75}O_4$, respectively. Using the Einstein−Smoluchowski equation[63] and the Li−Li jump distance of 1.76 Å (derived via MD hopping analysis) the respective diffusion coefficients D^T (at 573 K) are calculated to be 3.9×10^{-8}, 7.7×10^{-8}, and 6.1×10^{-8} cm^2/s for $Li_{3.75}Si_{0.75}P_{0.25}O_4$, $Li_{3.5}Si_{0.5}P_{0.5}O_4$, and $Li_{3.25}Si_{0.25}P_{0.75}O_4$, respectively. These values are again in line with the data and trends from the MD simulations.

3.3. Atomistic Conduction Mechanism. Of great interest to our present discussion is the question of the underlying

DOI: 10.1021/jacs.5b04444
J. Am. Chem. Soc. 2015, 137, 9136−9145

atomic-scale mechanism in the solid solutions that promotes enhanced conductivity. MD density plots of the accumulated lithium ion trajectories over the simulated time scale are a useful means of visualizing the migration pathways and the regions in the lattice which are most frequently traversed by the mobile Li^+ ions.

Lithium diffusion density plots are shown in Figure 12 for Li_3PO_4, Li_4SiO_4, and $Li_{3.5}Si_{0.5}P_{0.5}O_4$ at 573 K. First, it can be

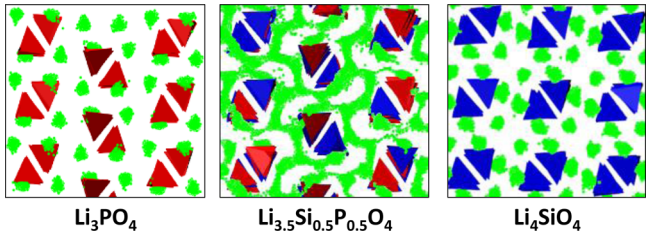

Figure 12. MD density plots of mobile lithium ions (green) overlaid on the tetrahedral framework structure (PO_4, red; SiO_4, blue) of Li_3PO_4, $Li_{3.5}Si_{0.5}P_{0.5}O_4$, and Li_4SiO_4.

seen that the trajectories in the mixed composition form a continuous 3D network of conduction pathways; this suggests that there is significantly greater Li^+ diffusion in the mixed composition than in the two end members. The 3D nature is important since the dimensionality of the Li^+ diffusion can have a major impact on the battery charge/discharge rate. For example, $LiFePO_4$ is a 1D conductor, and the presence of blocking defects in the 1D channels can severely impede the diffusion and the capacity.[43] In contrast, 3D diffusion behavior allows lithium access through all surfaces of the particles, irrespective of their crystallographic orientation, and would be less affected by blocking defects.

In previous studies[64,65] on the related Na_3PO_4 material, the contribution of tetrahedral rotation to ion conduction (termed the "paddle wheel" effect) has been discussed. To examine if such effects also operate in the Li_4SiO_4–Li_3PO_4 system, the movement of oxygen ions in the SiO_4/PO_4 tetrahedra during the MD simulation were plotted (Figure 13); it can be seen that the tetrahedra undergo only slight displacements, but with no major rotational motion to aid Li^+ conduction.

This result is in line with the findings of the ^{31}P NMR experiments. During the applied high-speed MAS experiments at 60 kHz using ambient temperature bearing and drive gas

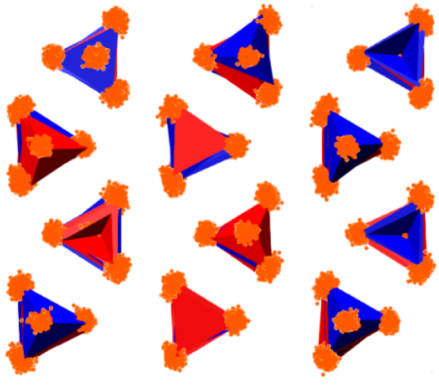

Figure 13. Density plots of oxygen atoms (orange) during the MD simulation overlaid on the tetrahedral framework structure of $Li_{3.5}Si_{0.5}P_{0.5}O_4$ (PO_4, red; SiO_4, blue).

flows the sample temperature is increased up to 70 °C.[66] However, the decrease of the MAS speed to 30 kHz (ca. 35 °C) and below does not affect the ^{31}P NMR signal line shape (SI, Figure S11), which indicates no significant movement of the anionic tetrahedra in this temperature regime.

Detailed analysis of ion transport from the MD simulations reveals that Li^+ diffusion takes place by a cooperative interstitialcy or knock-on type mechanism involving the concerted motion of interstitial and lattice Li^+ ions. This is illustrated in Figure 14 for $Li_{3.5}Si_{0.5}P_{0.5}O_4$, where continuous

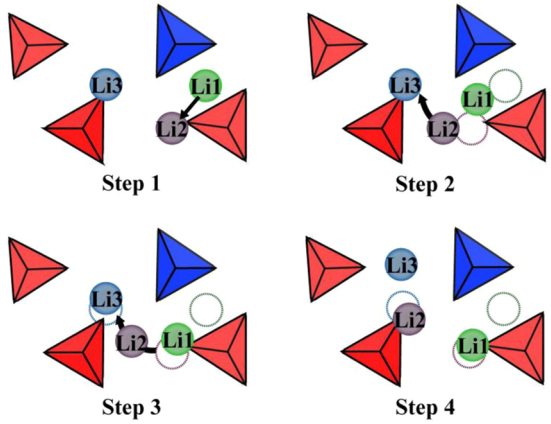

Figure 14. MD simulation snapshots of Li-ion positions in $Li_{3.5}Si_{0.5}P_{0.5}O_4$ showing the cooperative knock-on like mechanism: the migrating interstitial Li^+ (green) displaces another Li^+ (purple) toward a neighbor site which in turn leads to further Li^+ (blue) migration (PO_4, red; SiO_4, blue).

migration snapshots are presented, and shows the migrating interstitial Li ion displacing an adjacent Li ion into an interstitial position within the neighboring polyanion layer. Such a cooperative mechanism facilitates lithium-ion diffusion and promotes high ionic conductivity in these mixed Si/P compositions.

NMR studies[59,67] have reported lithium site exchange between different coordination environments, which is consistent with the mechanism presented here. Previous ab initio studies[68] of off-stoichiometric Li_3PO_4 set up with lithium interstitial defects find a low energy barrier for a Li^+ interstitialcy mechanism. Similar cooperative mechanisms have been suggested in other lithium-ion conductors,[46,69] and may be important in related framework-structured materials.[70]

As noted earlier, we have also analyzed the Haven ratio values to obtain a more quantitative assessment of the degree of correlated motion. For Li_3PO_4 a Haven ratio close to 1.0 at all temperatures is found (SI, Figure S18) suggesting uncorrelated ion motion, and consistent with the observed low conductivity. For Li_4SiO_4 correlated motion is not found at low temperatures (373 K) with a Haven ratio of 1.03; at elevated temperatures (473 K), as more lithium ions become mobile, some correlated motion is indicated with a Haven ratio reaching a value of 1.6. Given these results and the greater Li content of Li_4SiO_4, a high conductivity may be expected. However, the observed activation energy for lithium migration in Li_4SiO_4 is as high as 0.84 eV (Figure 11) indicating low mobility. For the mixed Si/P compositions we find higher Haven ratios in the range 2.3 to 3.6 (at 473 K) indicating significantly more correlated motion than in Li_4SiO_4, and consistent with the enhanced ionic conductivity that is experimentally observed.

DOI: 10.1021/jacs.5b04444
J. Am. Chem. Soc. 2015, 137, 9136–9145

On the basis of these insights, we suggest that further conductivity enhancement may be possible by disordering of the lithium sublattice via mixing or doping of the polyanion framework. We are currently exploring such avenues as well as synthesizing ^{6}Li-enriched samples of the solid solution to perform 1D and 2D exchange ^{6}Li NMR experiments.

4. CONCLUSIONS

This investigation of the Li_4SiO_4–Li_3PO_4 solid electrolyte system has used a powerful multi-technique approach of diffraction, AC impedance, NMR spectroscopy, and atomistic modeling to obtain new information concerning the crystal structures and lithium-ion conduction mechanisms. Several key features emerge:

(a) An immiscibility zone has been found for $(1-z)Li_4SiO_4$–$(z)Li_3PO_4$ compositions around $0.35 < z < 0.45$. Lower z compositions can be indexed to Li_4SiO_4-like structures, while higher z compositions are γ-Li_3PO_4-like. The crystal structures of the mixed compositions $Li_{3.5}Si_{0.5}P_{0.5}O_4$ and $Li_{3.25}Si_{0.25}P_{0.75}O_4$ have been determined for the first time, and can be described as isolated SiO_4 or PO_4 tetrahedra with a distribution of lithium atoms on multiple crystallographic sites. Such a disordered lithium sublattice is supported by ^{6}Li NMR results.

(b) Both AC impedance and MD simulation results for the $(1-z)Li_4SiO_4$–$(z)Li_3PO_4$ system reveal appreciable ionic conductivities (10^{-3} S/cm at 573 K) in the mixed compositions (z = 0.25, 0.5, 0.75), which are orders of magnitude higher than those of the end members. ^{7}Li and ^{31}P NMR results on local structure are in line with these findings and reveal the sensitivity of the activation energies to the local Li-ion dynamics.

(c) New fundamental understanding of the microscopic conduction mechanism is found. The MD simulations of the mixed Si/P compositions reveal Li-ion conduction pathways through 3D networks; they also show a cooperative-type interstitial mechanism, which is consistent with the Haven ratio values and the Li-ion dynamics from NMR. Such correlated motion is a key factor in promoting high ionic conductivity.

These insights are of great significance in developing strategies for optimizing the Li-ion conductivity of this system, as well as identifying new solid electrolytes.

■ ASSOCIATED CONTENT

Supporting Information

Single-crystal measurement results for Li_4SiO_4; BPP fit parameters and results; interatomic potentials; crystallographic data for solid solution compositions; comparison of calculated and experimental structural parameters; ^{7}Li ambient and high-temperature NMR signal line shapes and fwhm analysis; ^{6}Li and ^{31}P NMR signals; comparison of experimental and simulated structural parameters; AC impedance plots; ^{7}Li(T_1) vs T and Arrhenius plots; activation energies derived from NMR, AC impedance, and MD simulation; Arrhenius plots from MD and AC impedance; and Haven ratio values. The Supporting Information is available free of charge on the ACS Publications website at DOI: 10.1021/jacs.5b04444.

■ AUTHOR INFORMATION

Corresponding Author

*m.s.islam@bath.ac.uk

Notes

The authors declare no competing financial interest.

■ ACKNOWLEDGMENTS

The ALISTORE ERI and CNRS are acknowledged for supporting Y.D. through a joint Ph.D. scholarship between Picardie (France) and Bath (UK). The authors thank D. Sheptyakov (PSI, Switzerland) and M. Bianchini (ILL-Grenoble, France) for assistance with neutron diffraction experiments, and M. T. Dunstan (Cambridge, UK) for assistance with NMR experiments. Financial support from the EPSRC Energy Materials Programme (Grant EP/K016288) is gratefully acknowledged. The HPC Materials Chemistry Consortium (EP/L000202) allowed use of the ARCHER facilities. O.P. and S.E. acknowledge support from a Marie Skłodowska-Curie Fellowship (H2020-MSCA-IF-2014-EF, no. 655444) and an ERASMUS+ scholarship, respectively.

■ REFERENCES

(1) Kamaya, N.; Homma, K.; Yamakawa, Y.; Hirayama, M.; Kanno, R.; Yonemura, M.; Kamiyama, T.; Kato, Y.; Hama, S.; Kawamoto, K.; Mitsui, A. *Nat. Mater.* **2011**, *10*, 682–686.
(2) Masquelier, C. *Nat. Mater.* **2011**, *10*, 649–650.
(3) Quartarone, E.; Mustarelli, P. *Chem. Soc. Rev.* **2011**, *40*, 2525–2540.
(4) Fergus, J. W. *J. Power Sources* **2010**, *195*, 4554–4569.
(5) Kanno, R.; Murayama, M. *J. Electrochem. Soc.* **2001**, *148*, A742–A746.
(6) Mizuno, F.; Hayashi, A.; Tadanaga, K.; Tatsumisago, M. *Adv. Mater.* **2005**, *17*, 918–921.
(7) Goodenough, J. B.; Hong, H. Y.-P.; Kafalas, J. A. *Mater. Res. Bull.* **1976**, *11*, 203–220.
(8) Bruce, P. G.; West, A. R. *J. Electrochem. Soc.* **1983**, *130*, 662–669.
(9) Kanno, R.; Hata, T.; Kawamoto, Y.; Irie, M. *Solid State Ionics* **2000**, *130*, 97–104.
(10) Thangadurai, V.; Kaack, H.; Weppner, W. J. F. *J. Am. Ceram. Soc.* **2003**, *86*, 437–440.
(11) Cussen, E. J. *J. Mater. Chem.* **2010**, *20*, 5167–5173.
(12) Hull, S. *Rep. Prog. Phys.* **2004**, *67*, 1233–1314.
(13) Seino, Y.; Ota, T.; Takada, K.; Hayashi, A.; Tatsumisago, M. *Energy Environ. Sci.* **2014**, *7*, 627–631.
(14) Ong, S. P.; Mo, Y.; Richards, W. D.; Miara, L.; Lee, H. S.; Ceder, G. *Energy Environ. Sci.* **2013**, *6*, 148–156.
(15) Hu, Y.-W.; Raistrick, I. D.; Huggins, R. A. *J. Electrochem. Soc.* **1977**, *124*, 1240–1242.
(16) Huggins, R. A. *Electrochim. Acta* **1977**, *22*, 773–781.
(17) Shannon, R. D.; Taylor, B. E.; English, A. D.; Berzins, T. *Electrochim. Acta* **1977**, *22*, 783–796.
(18) Arachi, Y.; Higuchi, Y.; Nakamura, R.; Takagi, Y.; Tabuchi, M. *J. Power Sources* **2013**, *244*, 631–635.
(19) Kuwata, N.; Iwagami, N.; Tanji, Y.; Matsuda, Y.; Kawamura, J. *J. Electrochem. Soc.* **2010**, *157*, A521–A527.
(20) Xie, J.; Oudenhoven, J. F. M.; Harks, P.-P. R. M. L.; Li, D.; Notten, P. H. L. *J. Electrochem. Soc.* **2015**, *162*, A249–A254.
(21) Adnan, S. B. R. S.; Mohamed, N. S. *Solid State Ionics* **2014**, *262*, 559–562.
(22) Sumita, M.; Tanaka, Y.; Ikeda, M.; Ohno, T. *J. Phys. Chem. C* **2015**, *119*, 14–22.
(23) Lepley, N. D.; Holzwarth, N. A. W.; Du, Y. A. *Phys. Rev. B: Condens. Matter Mater. Phys.* **2013**, *88*, 104103.
(24) Santosh, K. C.; Longo, R. C.; Xiong, K.; Cho, K. *J. Electrochem. Soc.* **2014**, *161*, F3104–F3110.

DOI: 10.1021/jacs.5b04444
J. Am. Chem. Soc. 2015, 137, 9136–9145

(25) Kobayashi, Y.; Seki, S.; Yamanaka, A.; Miyashiro, H.; Mita, Y.; Iwahori, T. *J. Power Sources* **2005**, *146*, 719−722.
(26) Zhang, L.; Cheng, L.; Cabana, J.; Chen, G.; Doeff, M. M.; Richardson, T. J. *Solid State Ionics* **2013**, *231*, 109−115.
(27) Whitacre, J. F.; West, W. C. *Solid State Ionics* **2004**, *175*, 251−255.
(28) Völlenkle, H.; Wittmann, A.; Nowotny, H. *Monatsh. Chem.* **1968**, *99*, 1360−1371.
(29) Tranqui, D.; Shannon, R. D.; Chen, H. Y.; Iijima, S.; Baur, W. H. *Acta Crystallogr., Sect. B: Struct. Crystallogr. Cryst. Chem.* **1979**, *35*, 2479−2487.
(30) Khorassani, A.; Izquierdo, G.; West, A. R. *Mater. Res. Bull.* **1981**, *16*, 1561−1567.
(31) Mejía-Trejo, V. L.; Fregoso-Israel, E.; Pfeiffer, H. *Chem. Mater.* **2008**, *20*, 7171−7176.
(32) Blau, B.; Clausen, K. N.; Gvasaliya, S.; Janoschek, M.; Janssen, S.; Keller, L.; Roessli, B.; Schefer, J.; Tregenna-Piggott, P.; Wagner, W.; Zaharko, O. *Neutron News* **2009**, *20*, 5−8.
(33) Fischer, P.; Frey, G.; Koch, M.; Könnecke, M.; Pomjakushin, V.; Schefer, J.; Thut, R.; Schlumpf, N.; Bürge, R.; Greuter, U.; Bondt, S.; Berruyer, E. *Phys. B* **2000**, *276−278*, 146−147.
(34) Lalère, F.; Leriche, J. B.; Courty, M.; Boulineau, S.; Viallet, V.; Masquelier, C.; Seznec, V. *J. Power Sources* **2014**, *247*, 975−980.
(35) Bielecki, A.; Burum, D. *J. Magn. Reson., Ser. A* **1995**, *116*, 215−220.
(36) Harris, R. K.; Becker, E. D.; de Menezes, S. M. C.; Goodfellow, R.; Granger, P. *Solid State Nucl. Magn. Reson.* **2002**, *22*, 458−483.
(37) Asai, T.; Kawai, S. *Solid State Ionics* **1982**, *7*, 43−47.
(38) Asai, T.; Kawai, S. *Solid State Commun.* **1980**, *36*, 891−893.
(39) Eichele, K.; Wasylishen, R. E. *J. Phys. Chem.* **1994**, *98*, 3108−3113.
(40) Lewis, G. V.; Catlow, C. R. A. *J. Phys. C: Solid State Phys.* **1985**, *18*, 1149−1161.
(41) Gale, J. D.; Rohl, A. L. *Mol. Simul.* **2003**, *29*, 291−341.
(42) Todorov, I. T.; Smith, W.; Trachenko, K.; Dove, M. T. *J. Mater. Chem.* **2006**, *16*, 1911−1918.
(43) Islam, M. S.; Fisher, C. A. J. *Chem. Soc. Rev.* **2014**, *43*, 185−204.
(44) Pedone, A.; Malavasi, G.; Menziani, M. C.; Cormack, A. N.; Segre, U. *J. Phys. Chem. B* **2006**, *110*, 11780−11795.
(45) Catlow, C. R. A. *Annu. Rev. Mater. Sci.* **1986**, *16*, 517−548.
(46) Panchmatia, P. M.; Armstrong, A. R.; Bruce, P. G.; Islam, M. S. *Phys. Chem. Chem. Phys.* **2014**, *16*, 21114−21118.
(47) Adams, S.; Prasada Rao, R. *Solid State Ionics* **2011**, *184*, 57−61.
(48) Lee, S.; Park, S. S. *J. Phys. Chem. C* **2012**, *116*, 6484−6489.
(49) Roy, S.; Kumar, P. P. *Phys. Chem. Chem. Phys.* **2013**, *15*, 4965−4969.
(50) Armstrong, A. R.; Lyness, C.; Panchmatia, P. M.; Islam, M. S.; Bruce, P. G. *Nat. Mater.* **2011**, *10*, 223−229.
(51) Armstrong, A. R.; Kuganathan, N.; Islam, M. S.; Bruce, P. G. *J. Am. Chem. Soc.* **2011**, *133*, 13031−13035.
(52) Eames, C.; Islam, M. S. *J. Am. Chem. Soc.* **2014**, *136*, 16270−16276.
(53) Li, W.; Garofalini, S. H. *J. Electrochem. Soc.* **2005**, *152*, A364−A369.
(54) Morgan, B. J.; Madden, P. A. *Phys. Rev. Lett.* **2014**, *112*, 145901.
(55) De Jong, B. H. W. S.; Ellerbroek, D.; Spek, A. L. *Acta Crystallogr., Sect. B: Struct. Sci.* **1994**, *50*, 511−518.
(56) Baur, W. H.; Ohta, T. *J. Solid State Chem.* **1982**, *44*, 50−59.
(57) Yakubovich, O. V.; Urusov, V. S. *Crystallogr. Rep.* **1997**, *42*, 261−268.
(58) Baur, W. H. *Acta Crystallogr., Sect. B: Struct. Crystallogr. Cryst. Chem.* **1974**, *30*, 1195−1215.
(59) Xu, Z.; Stebbins, J. F. *Science* **1995**, *270*, 1332−1334.
(60) Xu, Z.; Stebbins, J. F. *Solid State Nucl. Magn. Reson.* **1995**, *5*, 103−112.
(61) Stebbins, J. F.; Xu, Z.; Vollath, D. *Solid State Ionics* **1995**, *78*, L1−L8.
(62) Smaihi, M.; Petit, D.; Gourbilleau, F.; Chaput, F.; Boilot, J. P. *Solid State Ionics* **1991**, *48*, 213−223.
(63) Indris, S.; Heitjans, P.; Uecker, R.; Roling, B. *J. Phys. Chem. C* **2012**, *116*, 14243−14247.
(64) Jansen, M. *Angew. Chem., Int. Ed. Engl.* **1991**, *30*, 1547−1558.
(65) Yin, W.-G.; Liu, J.; Duan, C.-G.; Mei, W.; Smith, R.; Hardy, J. *Phys. Rev. B: Condens. Matter Mater. Phys.* **2004**, *70*, 064302.
(66) Bruker BioSpin GmbH. *Very Fast MAS, MAS 1.3 mm User Guide*, Version 001; Probe Development Department, Rheinstetten, Germany, 2007.
(67) Wilkening, M.; Heitjans, P. *J. Phys.: Condens. Matter* **2006**, *18*, 9849−9862.
(68) Du, Y. A.; Holzwarth, N. a. W. *J. Electrochem. Soc.* **2007**, *154*, A999−A1004.
(69) Nishino, S.; Fujiwara, T.; Yamasaki, H. *Phys. Rev. B: Condens. Matter Mater. Phys.* **2014**, *90*, 024303.
(70) Fujimura, K.; Seko, A.; Koyama, Y.; Kuwabara, A.; Kishida, I.; Shitara, K.; Fisher, C. A. J.; Moriwake, H.; Tanaka, I. *Adv. Energy Mater.* **2013**, *3*, 980−985.

DOI: 10.1021/jacs.5b04444
J. Am. Chem. Soc. 2015, 137, 9136−9145